quantum beam science

MDPI

Article

Modification of SiO_2, ZnO, Fe_2O_3 and TiN Films by Electronic Excitation under High Energy Ion Impact

Noriaki Matsunami [1,*], Masao Sataka [2], Satoru Okayasu [2] and Bun Tsuchiya [1]

[1] Faculty of Science and Technology, Meijo University, Nagoya 468-8502, Japan; btsuchiya@meijo-u.ac.jp
[2] Japan Atomic Energy Agency (JAEA), Tokai 319-1195, Japan; sataka@tac.tsukuba.ac.jp (M.S.); okayasu.satoru@jaea.go.jp (S.O.)
* Correspondence: atsu20matsu@gmail.com

Abstract: It has been known that the modification of non-metallic solid materials (oxides, nitrides, etc.), e.g., the formation of tracks, sputtering representing atomic displacement near the surface and lattice disordering are induced by electronic excitation under high-energy ion impact. We have investigated lattice disordering by the X-ray diffraction (XRD) of SiO_2, ZnO, Fe_2O_3 and TiN films and have also measured the sputtering yields of TiN for a comparison of lattice disordering with sputtering. We find that both the degradation of the XRD intensity per unit ion fluence and the sputtering yields follow the power-law of the electronic stopping power and that these exponents are larger than unity. The exponents for the XRD degradation and sputtering are found to be comparable. These results imply that similar mechanisms are responsible for the lattice disordering and electronic sputtering. A mechanism of electron–lattice coupling, i.e., the energy transfer from the electronic system into the lattice, is discussed based on a crude estimation of atomic displacement due to Coulomb repulsion during the short neutralization time (~fs) in the ionized region. The bandgap scheme or exciton model is examined.

Keywords: electronic excitation; lattice disordering; sputtering; electron–lattice coupling

Citation: Matsunami, N.; Sataka, M.; Okayasu, S.; Tsuchiya, B. Modification of SiO_2, ZnO, Fe_2O_3 and TiN Films by Electronic Excitation under High Energy Ion Impact. *Quantum Beam Sci.* **2021**, *5*, 30. https://doi.org/10.3390/qubs5040030

Academic Editors: Akihiro Iwase and Rozaliya Barabash

Received: 30 August 2021
Accepted: 17 October 2021
Published: 27 October 2021

1. Introduction

Material modification induced by electronic excitation under high-energy (> 0.1 MeV/u) ion impact has been observed for many non-metallic solids since the late 1950's; for example, the formation of tracks (each track is characterized by a long cylindrical disordered region or amorphous phase in crystalline solids) in LiF crystal (photographic observation after chemical etching) by Young [1], in mica (a direct observation using transmission electron microscopy, TEM, without chemical etching, and often called a latent track) by Silk et al. [2], in SiO_2-quartz, crystalline mica, amorphous P-doped V_2O_5, etc. (TEM) by Fleischer et al. [3,4], in oxides (SiO_2-quartz, Al_2O_3, $ZrSi_2O_4$, $Y_3Fe_5O_{12}$, high-Tc superconducting copper oxides, etc.) (TEM) by Meftah et al. [5] and Toulemonde et al. [6], in Al_2O_3 crystal (atomic force microscopy, AFM) by Ramos et al. [7], in Al_2O_3 and MgO crystals (TEM and AFM) by Skuratov et al. [8], in Al_2O_3 crystal (AFM) by Khalfaoui et al. [9], in Al_2O_3 crystal (high resolution TEM) by O'Connell et al. [10], in amorphous SiO_2 (small angle X-ray scattering (SAXS)) by Kluth et al. [11], in amorphous SiO_2 (TEM) by Benyagoub et al. [12], in polycrystalline Si_3N_4 (TEM) by Zinkle et al. [13] and by Vuuren et al. [14], in amorphous $Si_{3.55}N_4$ (TEM) by Kitayama et al. [15], in amorphous $SiN_{0.95}$:H and $SiO_{1.85}$:H (SAXS) by Mota-Santiago et al. [16], in epilayer GaN (TEM) by Kucheyev et al. [17], in epilayer GaN (AFM) by Mansouri et al. [18], in epilayer GaN and InP (TEM) by Sall et al. [19], in epilayer GaN (TEM) by Moisy et al. [20], in InN single crystal (TEM) by Kamarou et al. [21], in SiC crystal (AFM) by Ochedowski et al. [22] and in crystalline mica (AFM) by Alencar et al. [23]. Amorphization has been observed for crystalline SiO_2 [5] and the Al_2O_3 surface at a high ion fluence (though the XRD peak remains) by Ohkubo et al. [24] and Grygiel et al. [25]. The counter process, i.e., the recrystallization of the amorphous or disordered regions, has been reported for SiO_2 by Dhar et al. [26], Al_2O_3 by Rymzhanov [27] and InP, etc., by Williams [28]. Density

modification, i.e., a lower density in the track core surrounded by a shell with a higher density, has been observed for Al_2O_3 [10], amorphous SiO_2 [11], Si_3N_4 [14] and amorphous $SiN_{0.95}$:H and $SiO_{1.85}$:H [16]. Interestingly, an electrically conducting track formation in tetrahedral-amorphous carbon (sp^3 into sp^2 bond transformation) has been observed by Gupta et al. [29]. The track radius, hillock height and diameter characterizing the surface morphology modification associated with the track are well described in terms of the electronic stopping power S_e (defined as the energy loss due to electronic excitation and ionization per unit path length), and the velocity effect has been noticed [12]. The threshold of S_e for the track formation has been reported [3,6,8,9,12,13,30] and the data appear to scatter, and it seems that the threshold S_e depends on the observation method of the track [12]. No track formation by monatomic ions has been observed in AlN [19].

Moreover, electronic sputtering (the erosion of solid materials caused by electronic energy deposition) has been observed for various compound solids: UO_2 by thermal-neutron-induced ^{235}U fission fragments by Rogers [31,32] and by Nilsson [33], UO_2 by energetic ions by Meins et al. [34], Bouffard et al. [35] and Schlutig [36], H_2O ice by Brown et al. [37,38], Bottiger et al. [39], Baragiola et al. [40], Dartois et al. [41] and Galli et al. [42], frozen gas films of Xe, CO_2 and SF_6 [39], those of CO, Ar and N_2 by Brown et al. [43], CO_2 ice by Mejia et al. [44], SiO_2 by Qui et al. [45], Sugden et. al. [46], Matsunami et al. [47,48], Arnoldbik et al. [49] and Toulemonde et al. [50,51], $MgAl_2O_4$ [48], UF_4 ([34], by Griffith et al. [52] and Toulemonde et al. [53]), $LiNbO_3$ [45], Al_2O_3 ([45] and by Matsunami et al. [54]), various oxides by Matsunami et al. ($SrTiO_3$ and $SrCeO_3$ [47,54], CeO_2, MgO, TiO_2 and ZnO [54], Y_2O_3 and ZrO_2 [55], Cu_2O [56,57], WO_3 [58], CuO [59], Fe_2O_3 [60]), Si_3N_4 [45], Si_3N_4 and AlN by Matsunami et al. [55], Cu_3N by Matsunami et al. [56,61], LiF ([50], by Assmann et al. [62] and Toulemonde et al. [63]), KBr [56], NaCl [63], CaF_2 [53] and SiC [56]. The sputtering of frozen Xe films has been observed for low energy electron impact, against the anticipation of no atomic displacement [39], and the result confirms that the sputtering is caused by electronic excitation. Mechanisms of electronic excitation leading to atomic displacement will be discussed in Section 4.

As mentioned above, electronic sputtering has been observed for a variety of non-metallic materials, indicating that it seems to be a general phenomenon for non-metallic solids by high-energy ion impact. In many cases, ions with an equilibrium charge have been employed, which is usually attained by inserting thin foils, such as carbon, metals, etc., before impact on samples, and sputtered atoms are collected in carbon, metals, etc., followed by neutron activation and ion beam analysis to obtain sputtering yields. This article concerns the equilibrium charge incidence, though charge-state effects for non-equilibrium charge incidence have been observed and discussed ([23,29,34,49,52,58,62,64]). The electronic energy deposition or electronic stopping power (S_e) at the equilibrium charge can be calculated using a TRIM or SRIM code by Ziegler et al. [65,66], a CasP code by Grande et al. [67] and the nuclear stopping power (S_n, defined as the energy loss due to elastic collisions per unit path length) [65,66]. Characteristic features of the electronic sputtering by high-energy ions are as follows:

(a). Electronic sputtering yields (Y_{SP}) are found to be larger by 10–10^3 than nuclear sputtering yields due to elastic collision cascades, which can be estimated assuming linear dependence on S_n;

(b). Y_{SP} super linearly depends on S_e and is approximated by the power-law fit: $Y_{SP} = (B_{SP}S_e)^{Nsp}$ with $1 \leqq N_{SP} \leqq 4$ for most cases, with B_{SP} being a material dependent constant.

Stoichiometric sputtering has been observed for many materials, whereas a considerable deviation from the stoichiometric sputtering has been reported for $YBa_2Cu_3O_7$ [68], $Gd_3Ga_5O_{12}$ and $Y_3Fe_5O_{12}$ [69] and CaF_2 and UF_4 [53]. Only the heavy element of U [31–36] and the light element of O [49] have been detected.

Besides track formation and electronic sputtering, lattice disordering (the degradation of X-ray diffraction (XRD) intensity) with lattice expansion (an increase in the lattice parameter) by high-energy ions has been observed for the polycrystalline films of SiO_2 [70] and WO_3 [58], and lattice disordering with lattice compaction for those of Cu_2O [57],

CuO [59], Fe_2O_3 [60], Cu_3N [61] and Mn-doped ZnO [71]. Only lattice disordering has been observed for the ultra-thin films of WO_3 [72]. It should be noted that a comparison between high-energy and low-energy ion impact effects is important. Lattice expansion has been observed for a few keV D ion irradiation on Fe_2O_3 [73], and this can be understood by the incorporation of D into non-substitutional sites (incorporation or implantation effect). Thus, lattice expansion by medium-energy ions (100 keV Ne) on Fe_2O_3 [60] could be understood by Ne incorporation and/or interstitial-type defects generated by ion impact, with a possible stabilization by incorporating Ne in the film, whereas lattice compaction has been observed for a 100 MeV Xe ion impact on Fe_2O_3 [60]. It should be noted that the incorporation of ions in thin films does not take place for high-energy ions, since the projected range of ions (R_p) is much larger than the film thickness (e.g., R_p of 14 μm for 100 MeV Xe in SiO_2), unless the thickness is too large. The lattice expansion due to the incorporation effect has been observed for a few keV H and D irradiation at a low fluence on WNO_x with $x \approx 0.4$, whereas lattice compaction has been observed at a high fluence of D [74]. Peculiarly, lattice expansion at a low ion fluence and compaction at a high fluence, as well as disordering, have been reported for medium-energy (100 keV Ne and N) and high-energy (100 MeV Xe and 90 MeV Ni) ion impact on WNO_x [75,76]. One speculation is that the lattice compaction is due to vacancy-type defects generated by ion impact, which is to be investigated. Furthermore, a drastic increase in electrical conductivity has been observed for Cu_3N [61], Mn-doped ZnO [71] and WNO_x with $x \approx 0.4$ [75,76]. The conductivity increase is ascribed to the increase in the carrier concentration and mobility.

There are a few reports on the S_e dependence of the XRD intensity degradation per unit fluence (Y_{XD}) for SiC and KBr [56] and WO_3 [72]. Y_{XD} is found to follow the power-law fit: $Y_{XD} = (B_{XD}S_e)^{N_{XD}}$, B_{XD} being a material-dependent constant and the exponent N_{XD} being comparable with the Nsp of the electronic sputtering. The results imply that similar mechanisms operate for lattice disordering and electronic sputtering. It is of interest to compare the S_e dependence of lattice disordering with that of electronic sputtering for materials other than those mentioned above. In this paper, we have measured the lattice disordering of SiO_2, ZnO, Fe_2O_3 and TiN films, and the sputtering of TiN. The XRD results are compared with the sputtering. The exciton model is examined and scaling parameters are explored for representing electronic excitation effects.

2. Materials and Methods

XRD has been measured using Cu-k_α radiation. Accuracy of the XRD intensity is estimated to be approximately 10%, based on the variation of repeated measurements. Rutherford backscattering (RBS) has been performed with MeV He ions for evaluation of film thickness and composition. Similarly, accuracy of the RBS is estimated considering the variation of the repeated measurements. High-energy ion irradiation has been performed at room temperature and normal incidence. Irradiation of high-energy ion with lower incident charge than the equilibrium charge without carbon foil is often employed for the samples of XRD measurement; however, the effect of non-equilibrium charge incidence does not come into play because the length for attaining the equilibrium charge is much smaller than the film thickness, as described for each material in Section 3.

SiO_2 films have been grown by thermal oxidation of Si(001) at 1300 °C for 5 hr. According to XRD, the films are polycrystalline with diffraction peaks at ~21°, 22°, 31°, 33°, 36° and 69°, with very weak peak at 44° and 47°. The peaks at ~21°, 22°, 44° and 47° have been assigned to (100), (002), (004) and (202) diffraction of hexagonal-tridymite structure [70]. The strong peak at 69° is Si(004) and peak at 33° is possibly Si(002). Film thickness is ~1.5 μm and the composition is stoichiometric (O/Si = 2.0 ± 5%) by RBS of 1.8 MeV He. Film density is taken to be the same as that of amorphous-SiO_2 (a-SiO_2), since it has been derived to be 2.26 gcm^{-3} from XRD results, which is close to that of a-SiO_2 (2.2 gcm^{-3})

Pure ZnO films have been prepared on MgO (001) substrate by using a radio frequency magnetron sputtering (RFMS) deposition method with ZnO target, and it has been reported that the dominant growth orientation is (001) and (100) of hexagonal-wurtzite structure

depending on the substrate temperature of 350 °C and 500 °C during the film growth, respectively [71,77,78]. The composition is stoichiometric, i.e., O/Zn = 1.0 ± 0.05, and film thickness is ~100 nm by He RBS. Here, the density is taken to be 4.2 × 10^{22} Zn cm^{-3} (5.67 gcm^{-3}).

Preparation and characterization methods of Fe_2O_3 films are described in [60]. Briefly, Fe_2O_3 films have been prepared by deposition of Fe layers on SiO_2-glass and C-plane cut Al_2O_3 (C-Al_2O_3) substrates using a RFMS deposition method with Fe target (99.99%) and Ar gas, followed by oxidation at 500 °C for 2–5 hr in air. According to RBS of 1.4–1.8 MeV He ions, the composition is stoichiometric (O/Fe = 1.5 ± 0.1) and film thickness used in this study is ~100 nm. Here, the density of 3.96 × 10^{22} Fe cm^{-3} (5.25 gcm^{-3}) is employed. Diffraction peaks have been observed at ~33° and 36°, and crystalline structure has been identified as hexagonal Fe_2O_3 (hematite or α-Fe_2O_3). These correspond to (104) and (110) diffraction planes.

TiN films have been prepared on SiO_2-glass, C-plane cut Al_2O_3 (C-Al_2O_3) and R-plane cut Al_2O_3 (R-Al_2O_3) substrates at 600°C using a RFMS deposition method with Ti target (99.5%) and high purity N_2 gas. RBS of 1.4–1.8 MeV He ions shows that the composition is stoichiometric (N/Ti = 1.0 ± 0.05) and that the film thickness used in this study is ~170 nm (deposition time of 1 hr). Here, the density of 5.25x10^{22} Ti cm^{-3} (5.4 gcm^{-3}) is employed. Diffraction peaks have been observed at 36.6°, 42.6° and ~77° on SiO_2 glass and C-Al_2O_3. Crystalline structure has been identified as a cubic structure and these correspond to (111), (200) and (222) diffractions [79]. Diffraction intensity of (111) is larger than that of (200) on SiO_2 glass, and diffraction of (111) on C-Al_2O_3 is very intensive. TiN on R-Al_2O_3 has preferential growth orientation of (220) of a cubic structure (diffraction angle at ~61°). Sputtered atoms are collected in the carbon foil (100 nm) and the sputtered atoms are analyzed by RBS to obtain the sputtering yields [54] (carbon collector method).

3. Results and Discussion

3.1. SiO_2

The XRD intensity at the diffraction angle of ~22° (the most intensive (002) diffraction of hexagonal-trydimite) normalized to that of as-grown SiO_2 films on Si(001) is shown in Figure 1 as a function of the ion fluence for 90 MeV Ni^{+10}, 100 MeV Xe^{+14} and 200 MeV Xe^{+14} ion impact. The XRD intensity of the irradiated sample normalized to that of the unirradiated sample is proportional to the ion fluence to a certain fluence. Deviation from the linear dependence for the high fluence could be due to the overlapping effect. As observed in latent track formation (e.g., [5,6]), electronic excitation effects extend to a region (approximately cylindrical) with a radius of several nm and a length of the projected range or film thickness, and thus ions may hit the ion-irradiated part for a high ion fluence (called the overlapping effect). As described below, the XRD degradation yield per unit ion fluence (Y_{XD}) is reduced at a high fluence, and this could be understood as thermal annealing and/or a reduction in the disordered regions via ion-induced defects (recrystallization [26]). The damage cross-sections (A_D obtained by RBS-channeling (RBS-C) technique and TEM [5]) are compared with Y_{XD} in Figure 2, and it appears that both agree well for S_e > 10 keV. A discrepancy between A_D and Y_{XD} is seen for S_e < 10 keV, and the reason for this is not understood. In addition, sputtering yields are often reduced, and this is unlikely to be explained by the annealing effect. Therefore, the reasons for the sputtering suppression at a high fluence remain in question. The XRD degradation yields (Y_{XD}) per unit ion fluence are obtained and given in Table 1. The film thickness has been obtained to be ~1.5 μm, using 1.8 MeV He RBS. The attenuation length (L_{XA}) of Cu-k_α (8.0 keV) is obtained to be 128 μm [80] and the attenuation depth (L_{XA}·sin(22°/2)) = 24.3 μm. The film thickness (~1.5 μm) is much smaller than the attenuation depth and thus no correction is necessary for the XRD intensity. The lattice expansion or increase in the lattice parameter of 0.5% with an estimated error of 0.2% at 1 × 10^{12} cm^{-2} is found to be nearly independent of the electronic stopping power.

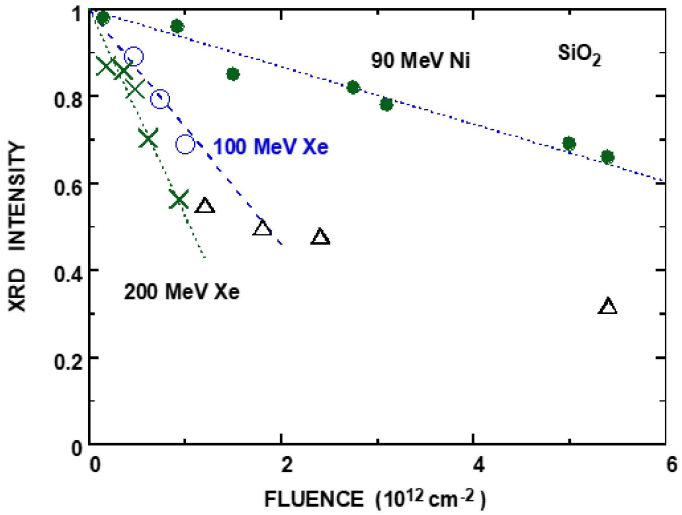

Figure 1. XRD intensity from (002) diffraction plane at ~22° normalized to as-grown films of SiO_2 as a function of ion fluence for 90 MeV Ni (•), 100 MeV Xe (o, Δ) and 200 MeV Xe (x) ions. Data of 90 MeV Ni (•) and 100 MeV Xe (Δ) are from [70]. Linear fit is indicated by dashed lines. An estimated error of XRD intensity is 10%.

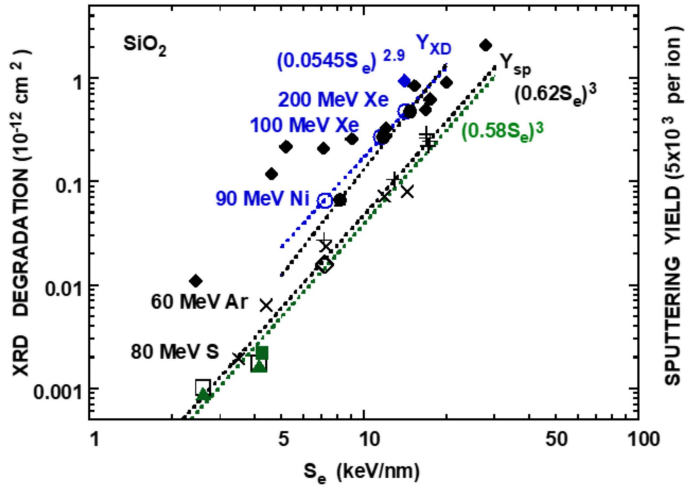

Figure 2. XRD degradation per unit fluence Y_{XD} of polycrystalline SiO_2 film (o, present result) and sputtering yield Ysp (x) of amorphous (or vitreous)-SiO_2 (□, x)) and film of SiO_2 (▲, ■, x, ◊, +) as a function of electronic stopping power (S_e). Data (□, ▲) from (Qiu et al.) [45], (■) from (Sugden et al.) [46], (x) from (Matsnami et al.) [47,48], (◊) from (Arnoldbik et al.) [49] and (+) from (Toulemonde et al.) [51]. S_e is calculated using SRIM2013, and power-law fits of Y_{XD} ($(0.0545S_e)^{2.9}$) and Y_{sp} ($(0.62S_e)^{3.0}$) are indicated by blue and black dotted lines, respectively. Power-law fit (•) Y_{XD} ($(0.055S_e)^{3.4}$, TRIM1997) and Y_{sp} ($(0.58S_e)^{3.0}$, TRIM1985 through SRIM2010) from [47,48,51] are indicated by black and green dashed lines. Damage cross sections (⧫) are obtained by RBS-C and (⧫) by TEM from [5].

Table 1. XRD data of SiO_2 films. Ion, incident energy (E in MeV), XRD intensity degradation (Y_{XD}), appropriate E* (MeV) considering the energy loss in the film and electronic stopping power in keV/nm (S_e*) appropriate for Y_{XD} (see text). S_e from SRIM2013. The deviation $\Delta S_e^* = (S_e^*/S_e(E) - 1) \times 100$ is also given.

Ion	Energy	Y_{XD}	E*	S_e*	ΔS_e*
	(MeV)	(10^{-12} cm^2)	(MeV)	(keV/nm)	(%)
^{58}Ni	90	0.066	84.5	7.246	−0.32
^{136}Xe	100	0.27	91.0	11.56	−3.2
^{136}Xe	200	0.475	189	14.22	−1.3

The electronic stopping power (S_e*) appropriate for XRD intensity degradation is calculated using SRIM 2013, using a half-way approximation that the ion loses its energy for half of the film thickness (~0.75 μm), i.e., $S_e^* = S_e(E^*)$ with E* = E(incidence) − S_e(E) × 0.75 μm (Table 1). The correction for the film thickness on S_e appears to be a few percent. It is noticed that the incident charge (Ni^{+10}, Xe^{+14}) differs from the equilibrium charge (+19, +25 and +30 for 90 MeV Ni, 100 MeV Xe and 200 MeV Xe, respectively (Shima et al.) [81], and +18.2, +23.9 and +29.3 (Schiwietz et al.) [82]), both being in good agreement. Following [64], the characteristic length (L_{EQ} = 1/(electron loss cross-section times N)) for attaining the equilibrium charge is estimated to be 8.7, 8.3 and 7.9 nm for 90 MeV Ni^{+10}, 100 MeV Xe^{+14} and 200 MeV Xe^{+14}, respectively, from the empirical formula of the single-electron loss cross-section σ_{1L} (10^{-16} cm^2) of 0.52 (90 MeV Ni^{+10}), 0.55 (100 MeV Xe^{+14}) and 0.57 (200 MeV Xe^{+14}) [83,84], N (2.2 × 10^{22} Si cm^{-3}) being the density, and (target atomic number)$^{2/3}$ dependence being included. Here, $\sigma_{1L} = \sigma_{1L}(Si) + 2\sigma_{1L}(O)$, ionization potential I_P = 321 eV [85,86] with the number of removable electrons N_{eff} = 8 and I_P = 343 eV with N_{eff} = 12 are employed for Ni^{+10} and Xe^{+14}. L_{EQ} is much smaller than the film thickness and hence the charge-state effect is insignificant.

The sputtering yields Y_{sp} of SiO_2 (normal incidence) are summarized in Table 2 for the comparison of the S_e dependence of the XRD degradation yields Y_{XD}. There are various versions of TRIM/SRIM starting in 1985, and in this occasion, the results used the latest version of SRIM2013 are compared with those earlier versions. Firstly, the correction on the stopping power and projected range for carbon foils (20–120 nm), which have been used to achieve the equilibrium charge incidence, is less than a few %, except for low-energy Cl ions (several %). Secondly, S_e by CasP (version 5.2) differs ~30% from that by SRIM 2013. Figure 2 shows the S_e dependence of the XRD degradation yields Y_{XD} and Y_{sp}. Both Y_{XD} and Y_{sp} fit to the power-law of S_e, and the exponents of XRD degradation N_{XD} = 2.9 and N_{sp} = 3 (sputtering) are almost identical, indicating that the same mechanism is responsible for lattice disordering and sputtering. Further plotted is the sputtering yields vs. S_e calculated using earlier versions of TRIM/SRIM (TRIM1985 to SRIM2010) [45–49,51], and the plot using earlier versions give the same exponent (N_{sp} = 3) with a 6% smaller constant B_{sp} in the power-law fit (20% smaller in the sputtering yields). This means that the plot and discussion using SRIM2013 do not significantly differ from those using the earlier versions of TRIM/SRIM. One notices that no appreciable difference in sputtering yields is observed among a-SiO_2, films and single-crystal-SiO_2 (c-SiO_2) [45–48], even though the density of c-SiO_2 is larger by 20% than that of a-SiO_2, whereas much smaller yields (by a factor of three) have been observed for c-SiO_2 [51]. The discrepancy remains in question. Sputtering yields Y_{EC}, which are due to elastic collision cascades, is estimated assuming Y_{EC} is proportional to the nuclear stopping power, discarding the variation of the α-factor (order of unity) depending on the ratio of target mass over ion mass (Sigmund) [87]. The proportional constant is obtained to be 2.7 nm/keV using the sputtering yields by low-energy ions (Ar and Kr) (Betz et al.) [88]. Y_{EC} is given in Table 2 and it is shown that Ysp/Y_{EC} ranges from 44 (5 MeV Cl) to 3450 (210 MeV Au).

Table 2. Sputtering data of SiO_2 (normal incidence). Ion, incident energy (E in MeV), energy (E* in MeV) corrected for the energy loss in carbon foils (see footnote), electronic stopping power (S_e), nuclear stopping power (S_n), projected range (R_p) and sputtering yield (Y_{SP}). S_e, S_n and R_p are calculated using SRIM2013. $(S_e(E^*)/S_e(E) - 1)$, $(S_n(E^*)/S_n(E) - 1)$ and $(R_p(E^*)/R_p(E) - 1)$ in % are given in the parentheses after $S_e(E^*)$, $S_n(E^*)$ and $R_p(E^*)$, respectively. Y_{SP} in the parenthesis is for SiO_2 films. $S_e(E)$ by CasP is also listed. Y_{EC} is the calculated sputtering yield due to elastic collisions.

Ion	E(E*)	$S_e(E^*)$	$S_n(E^*)$	$R_p(E^*)$	Y_{SP}	S_e(CasP)	Y_{EC}
	(MeV)	(keV/nm)	(keV/nm)	(μm)		(keV/nm)	
			Qiu et al. [45]				
^{35}Cl	5 (4.6)	2.59 (−4.26)	0.0426 (6.8)	3.0 (−4.6)	5.1 (4.4)	1.87	0.12
^{35}Cl	20 (19.4)	4.15 (−0.35)	0.0134 (2.7)	7.0 (−2.0)	8.77 (8.22)	3.83	0.036
			Sugden et al. [46]				
^{35}Cl	30 (29.9)	4.24 (−2.4 × 10^{-3})	9.3 × 10^{-3} (0.3)	9.5 (−0.25)	11	3.99	0.025
			Matsunami et al. [47,48]				
^{58}Ni	90 (89)	7.265 (−0.055)	0.0145 (0.84)	18.3 (−0.60)	120	7.66	0.039
^{136}Xe	100 (99)	11.88 (−0.49)	0.091 (1.2)	14.4 (−0.83)	362	14.0	0.246
^{136}Xe	200 (198)	14.37 (−0.19)	0.051 (0.73)	21.9 (−0.51)	404	16.0	0.138
^{40}Ar	60 (60)	4.40	6.5 × 10^{-3}	16.3	32	4.19	0.018
^{32}S	80 (80)	3.49	3.3 × 10^{-3}	23	9.7	3.23	0.0089
			Arnoldbik et al. [49]				
^{63}Cu	50 (50)	7.17	0.027	11.6	80	7.55	0.073
			Toulemonde et al. [51]				
^{197}Au	190 (190)	16.9	0.143	20.5	1425	20.9	0.39
^{197}Au	190 (190)				1320		
^{197}Au	197 (197)	17.1	0.14	20.9	1110	21.2	0.38
^{197}Au	210 (210)	17.4	0.13	21.7	1230	21.7	0.36
^{127}I	148 (148)	12.9	0.06	20	525	15.3	0.16
^{58}Ni	69 (69)	7.15	0.018	15.5	135	7.75	0.049

Equilibrium charge has been obtained by using carbon foils of 120 nm [45], 25 nm [46], 100 nm [47,48], 20 nm [49] and 50 nm [51].

In order to obtain the stopping powers (S) for the non-metallic compounds, such as SiO_2, described above, we apply the Bragg's additive rule, e.g., $S(SiO_2) = S(Si) + 2S(O)$ and S of the constituting elements is calculated using TRIM/SRIM and CasP codes. Before moving to the discussion of the Bragg's deviation, the accuracy of S is briefly mentioned. It is estimated to be 8% (Be through U ions in Ag) near the maximum of S (~0.8 MeV/u) [66], 17% (K to U ions in Au) (Paul) [89]. Besenbacher et al. have reported no difference between solid and gas phases for 0.5–3 MeV He ion stopping in Ar with an experimental accuracy of 3% [90], and this could be understood by the fact that the binding energy (cohesive energy) of solid Ar is too small (0.08 eV (Kittel) [91]), compared with the ionization potential (I_{Bethe}) of 188 eV [92], to affect the stopping. On the other hand, Arnau et al. have reported a large deviation (~50% near the stopping power maximum at ~50 keV) for proton stopping between solid and gas phases of Zn, and the deviation reduces ~10% at ~1 MeV [93]. The cohesive energy of 1.35 eV [91] is much smaller than the mean ionization potential I_{Bethe} of 330 eV [92], and hence the small increase in I_{Bethe} cannot explain the Bragg's deviation of Zn. They have argued that the difference in the 4s into 4p transition probability and screening effect between solid and gas phases are responsible. Both TRIM/SRIM and CasP codes are based on the experiments of conveniently available solid targets and molecular gas (e.g., N_2, O_2), and thus it is anticipated that the binding effect is included to some or large extent and that the Bragg's deviation is not serious for nitrides and oxides, and is roughly 10% or less at around 1 MeV/u.

3.2. ZnO

The XRD intensity at a diffraction angle of ~34° ((001) diffraction) and 32° ((100) diffraction) normalized to those of unirradiated ZnO films on the MgO substrate is shown in Figure 3 as a function of the ion fluence for 90 MeV Ni^{+10}, 100 MeV Xe^{+14} and 200 MeV Xe^{+14} ion impact. It appears that the XRD intensity degradation is nearly independent of the diffraction planes. The XRD intensity degradation per unit fluence Y_{XD} is given in Table 3, together with sputtering yields [54], stopping powers and projected ranges (SRIM2013). The X-ray (Cu-kα) attenuation length L_{XA} is obtained to be 36.6 μm [80] and the attenuation depth is 11 and 10 μm for the diffraction angle of ~34° and 32°, respectively; thus, the X-ray attenuation correction is unnecessary. It appears that the appropriate energy for the Y_{XD} vs. S_e plot, $E - S_e\ell/2$, where ℓ = a film thickness of ~100 nm, is nearly the same as E* for sputtering, in which the energy loss of a carbon foil of 100 nm is considered. Similarly to the case of SiO_2, the characteristic length (L_{EQ}) is estimated to be 4.6, 4.4 and 4.2 nm for 90 MeV Ni^{+10}, 100 MeV Xe^{+14} and 200 MeV Xe^{+14}, respectively, from the empirical formula of the single-electron loss cross-section $\sigma_{1L}(10^{-16}$ $cm^2)$ of 0.52 (90 MeV Ni^{+10}), 0.54 (100 MeV Xe^{+14}) and 0.57 (200 MeV Xe^{+14}) [83,84]. Here, $\sigma_{1L} = \sigma_{1L}(Zn) + \sigma_{1L}(O)$, and the ionization potential I_P and N_{eff} are described in Section 3.1. Again, L_{EQ} is much smaller than the film thickness and the charge-state effect is insignificant.

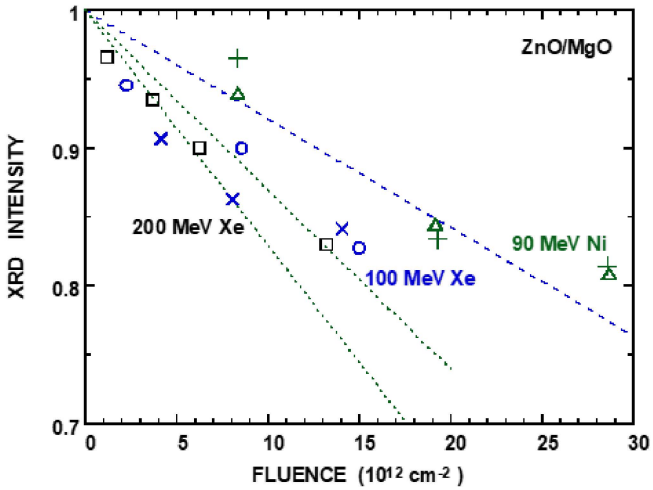

Figure 3. XRD intensity normalized to as-deposited films of ZnO as a function of ion fluence for 90 MeV Ni (Δ, +), 100 MeV Xe (o, x) and 200 MeV Xe (□) ions. Diffraction planes are (002) at ~34° (Δ, o, □) and (100) at ~32° (+, x). Linear fit is indicated by dashed lines. An estimated error of XRD intensity is 10%.

Table 3. XRD data of ZnO films. Ion, incident energy (E in MeV), XRD intensity degradation (Y_{XD}), E* = E − ΔE (energy loss in carbon foil of 100 nm) (MeV) and electronic (S_e*) and nuclear (S_n*) stopping powers in keV/nm and projected range R_p* (μm) at E* calculated using SRIM2013. Sputtering yield Y_{sp} from [54]. Sputtering yield by 100 keV Ne ion is also given.

Ion	Energy	Y_{XD}	E*	S_e*	S_n*	R_p*	Y_{sp}
	(MeV)	(10^{-14} cm^2)	(MeV)	(keV/nm)	(keV/nm)	(μm)	
^{32}S	80		80	6.62	0.007	13	1.09
^{40}Ar	60		60	8.3	0.014	9.5	2.08
^{58}Ni	90	0.788	89	13.72	0.031	11	4.0
^{127}I	85		84	18.92	0.205	8.8	7.0
^{136}Xe	100	1.3	99	21.60	0.20	8.8	
^{136}Xe	200	1.7	198	27.14	0.112	13	11
^{20}Ne	0.10	0.10		0.29	0.24	0.12	0.9

Figure 4 shows the XRD intensity degradation Y_{XD} vs. electronic stopping power (S_e) (SRIM2013 and TRIM1997) together with the sputtering yields Y_{sp} vs. S_e. Both Y_{XD} and Y_{sp} follow the power-law fit and the exponent for Y_{XD} using TRIM1997 gives a slightly larger value than that using SRIM2013. The exponent of lattice disordering is nearly the same as that of sputtering. The change in the lattice parameter $\Delta\ell c$ appears to scatter, and roughly -0.2% and -0.1% with an estimated error of 0.1% are obtained for (100) and (002) diffractions by 100 MeV Xe at 10×10^{12} cm^{-2}, assuming that $\Delta\ell c$ is proportional to the ion fluence. $\Delta\ell c$ is obtained at -0.3% for (002) diffraction by 200 MeV Xe at 5×10^{12} cm^{-2}, and no appreciable change in the lattice parameter is observed by 90 MeV Ni ions at 40×10^{12} cm^{-2}; more data are desired.

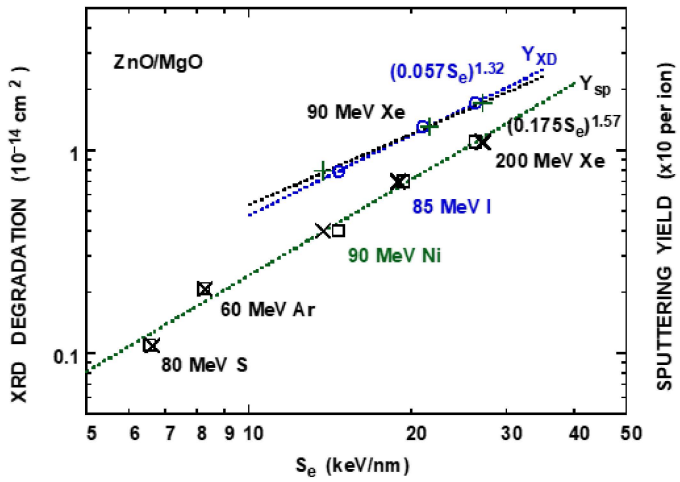

Figure 4. XRD degradation per unit fluence Y_{XD} of polycrystalline ZnO film vs. electronic stopping power S_e (TRIM1997 and SR2013). Power-law fit to $Y_{XD} = (0.057S_e)^{1.32}$ (TRIM1997) (o, blue dotted line) and $(0.0585\ S_e)^{1.16}$ (SRIM2013) (+, black dotted line). Sputtering yield Ysp vs. S_e (TRIM1997, □) and S_e (SR2013, x) is also shown. Sputtering yield from [54]. Power-law fits to Ysp: $(0.175\ S_e)^{1.57}$ for both S_e from TRIM1997 and SR2013 is indicated by green dotted line.

3.3. Fe_2O_3

The XRD intensity at a diffraction angle of ~33° and 36° (corresponding to diffraction planes of (104) and (110)) normalized to those of unirradiated Fe_2O_3 films on C-Al_2O_3 and SiO_2 glass substrates as a function of the ion fluence is shown in Figure 5 for 90 MeV Ni^{+10}, 100 MeV Xe^{+14} and 200 MeV Xe^{+14} ion impact. It appears that the XRD intensity degradation is nearly independent of the diffraction planes and substrates. The XRD intensity degradation per unit fluence Y_{XD} is given in Table 4, together with the sputtering yields [60] and stopping powers (SRIM2013). The X-ray (Cu-kα) attenuation length L_{XA} is obtained to be 8.8 μm [80] and the attenuation depth is 2.5 and 2.7 μm for the diffraction angle of ~33° and 36°, respectively, which are much larger the film thickness of ~100 nm and thus the X-ray attenuation correction is unnecessary. The appropriate energy for the XRD vs. S_e plot, using half-way approximation ($E - S_e\ell/2$) with the film thickness ℓ of ~100 nm, again gives nearly the same as E* for sputtering, in which the energy loss of the carbon foil of 100 nm is taken into account.

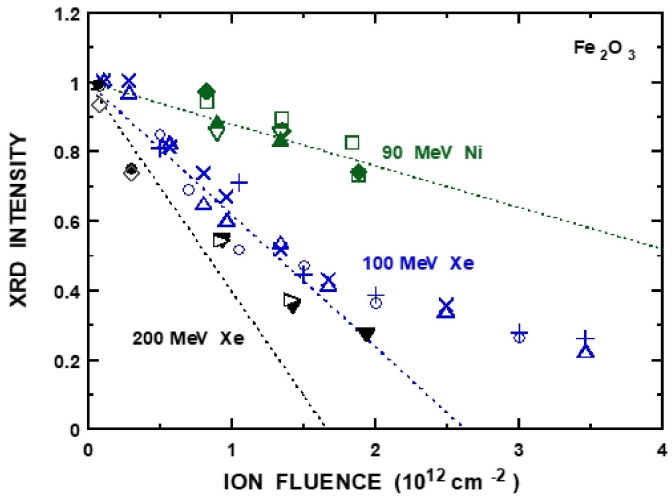

Figure 5. XRD intensity normalized to unirradiated films of Fe_2O_3 as a function of ion fluence for 90 MeV Ni (□, •, ▽, ▲), 100 MeV Xe (o, Δ, +, x) and 200 MeV Xe (•, ◊, ▼, ⋂) ions. Diffraction peaks at ~33° of Fe_2O_3 films on C-Al_2O_3 substrate (□ (90 MeV Ni), o (100 MeV Xe), • (200 MeV Xe)), ~36° of films on C-Al_2O_3 (• (90 MeV Ni), + (100 MeV Xe), ◊ (200 MeV Xe)), ~33° of films on SiO_2 glass substrate (▽ (90 MeV Ni), Δ (100 MeV Xe), ▼ (200 MeV Xe)) and ~36° of films on SiO_2 glass substrate (▲ (90 MeV Ni), x (100 MeV Xe), ⋂ (200 MeV Xe)). Data of 100 MeV Xe are from [60]. Linear fit is indicated by dotted lines. An estimated error of XRD intensity is 10%.

Table 4. XRD data of Fe_2O_3 films. Ion, energy (E in MeV), XRD intensity degradation (Y_{XD}), E* = E-ΔE (energy loss in carbon foil of 100 nm) (MeV) and electronic (S_e*) and nuclear (S_n*) stopping powers in keV/nm and projected range R_p* (μm) calculated using SRIM2013. Sputtering yield Y_{sp} from [60]. Results by low energy (100 keV Ne) ion are also given.

Ion	Energy	Y_{XD}	E*	S_e*	S_n*	R_p*	Y_{sp}
	(MeV)	(10^{-12} cm^2)	(MeV)	(keV/nm)	(keV/nm)	(μm)	
^{58}Ni	90	0.12	89	14.28	0.030	9.8	38.3
^{136}Xe	100	0.38	99	23.25	0.19	7.9	57.9
^{136}Xe	200	0.60	198	28.27	0.11	11.7	81.7
^{20}Ne	0.10		0.10	0.354	0.258	0.12	2.3

Similarly to SiO_2 and ZnO, the characteristic length (L_{EQ}) is estimated to be 4.5, 4.3 and 4.1 nm for 90 MeV Ni^{+10}, 100 MeV Xe^{+14} and 200 MeV Xe^{+14}, respectively, from the empirical formula of the single-electron loss cross-section σ_{1L}(10^{-16} cm^2) of 0.56 (90 MeV Ni^{+10}), 0.59 (100 MeV Xe^{+14}) and 0.61 (200 MeV Xe^{+14}) [83,84]. Here, $\sigma_{1L} = \sigma_{1L}$(Fe) + $1.5\sigma_{1L}$(O). L_{EQ} is much smaller than the film thickness and the charge-state effect does not come into play.

Figure 6 shows XRD intensity degradation Y_{XD} vs. electronic stopping power (S_e) (SRIM2013 and TRIM1997) together with the sputtering yields Y_{sp} vs. S_e. Both Y_{XD} and Y_{sp} follow the power-law fit and the exponent using TRIM1997 gives a slightly larger fit than those using SRIM2013. The exponent of lattice disordering is two times larger than that of sputtering (N_{sp} is exceptionally close to unity, in contrast to the SiO_2 and ZnO cases). The change in the lattice parameter appears to scatter depending on the substrate and diffraction planes, and is not proportional to the ion fluence. The average of the lattice parameter change in the (104) and (110) diffractions of Fe_2O_3 on C-Al_2O_3 is −0.2, −0.3% (an estimated error of 0.1%) and nearly zero at ~1 × 10^{12} cm^{-2} for 200 MeV Xe, 100 MeV Xe and 90 MeV Ni ion impact. The dependence of the lattice parameter change on the ion fluence and S_e is complicated, and is to be investigated.

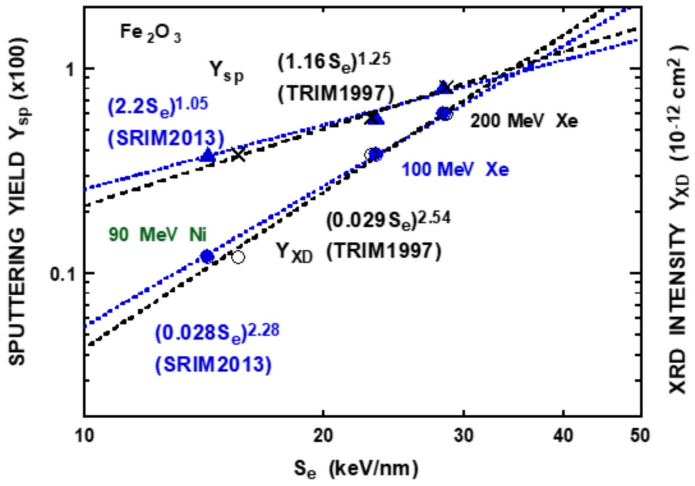

Figure 6. XRD dgradation per unit fluence Y_{XD} of polycrystalline Fe_2O_3 films (●, o) and sputtering yield Ysp (▲, x) as a function of the electronic stopping power (S_e) in keV/nm. Power-law fits are indicated by dashed lines and S_e is calculated using SRIM2013 (●, ▲) and TRIM1997 (o, x): (●) $Y_{XD} = (0.028\ S_e)^{2.28}$ (SRIM2013), (o) $Y_{XD} = (0.029 S_e)^{2.54}$ (TRIM1997), (▲) $Y_{sp} = (2.2\ S_e)^{1.05}$ (SRIM2013) and (x) $Y_{sp} = (1.16\ S_e)^{1.25}$ (TRIM1997). Sputtering data and power-law fit to the sputtering yields (TRIM1997) from [60].

3.4. TiN

The XRD patterns are shown in Figure 7 for unirradiated and irradiated TiN films on the SiO_2 glass substrate. As already mentioned in Section 2, (111) and (200) diffraction peaks are observed and the XRD intensity decreases due to ion impact. Figure 8 shows XRD intensities normalized to those of unirradiated TiN films on SiO_2 glass, C-Al_2O_3 and R-Al_2O_3 substrates as a function of the ion fluence. It is seen that the XRD intensity degradation is nearly the same for the diffraction planes of (111) and (200) on SiO_2, and for (111) on C-Al_2O_3. The XRD intensity degradation is less sensitive to the ion impact for the diffraction plane (220) on the R-Al_2O_3 substrate (~30% smaller than that for (111) and (200) on SiO_2, and for (111) on C-Al_2O_3). The XRD intensity degradation per unit fluence Y_{XD} for (111) and (200) diffractions is given in Table 5, together with sputtering yields and stopping powers (TRIM1997 and SRIM2013). No appreciable change in the lattice parameter is observed, as shown in Figure 7. Similarly to the SiO_2, ZnO and Fe_2O_3 cases, the appropriate energy, $E - S_e\ell/2$, ℓ = film thickness of ~170 nm is taken into account, and the energy is close to that for sputtering, in which the energy loss of the carbon foil of 100 nm is considered. The X-ray (Cu-kα) attenuation length L_{XA} is obtained to be 11.8 μm [80], and the attenuation depth is 3.7, 4.3 and 6.0 μm for diffraction angles of 36.6°, ~43° and 61°, respectively; thus, the X-ray attenuation correction is insignificant.

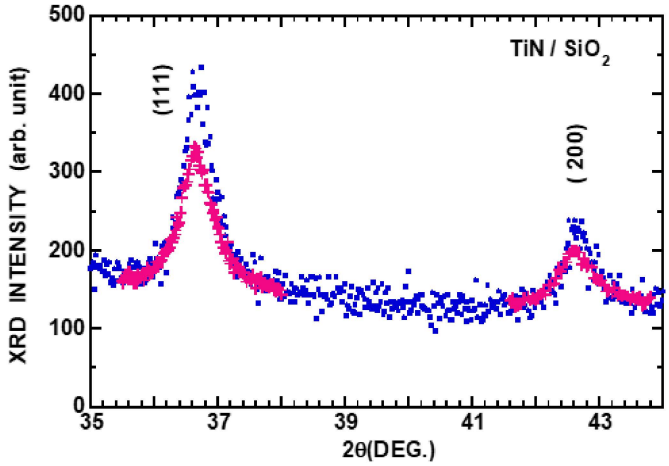

Figure 7. XRD patterns of TiN film on SiO_2 glass substrate: unirradiated (•) and irradiated by 100 MeV Xe at 0.72×10^{12} cm^{-2} (+).

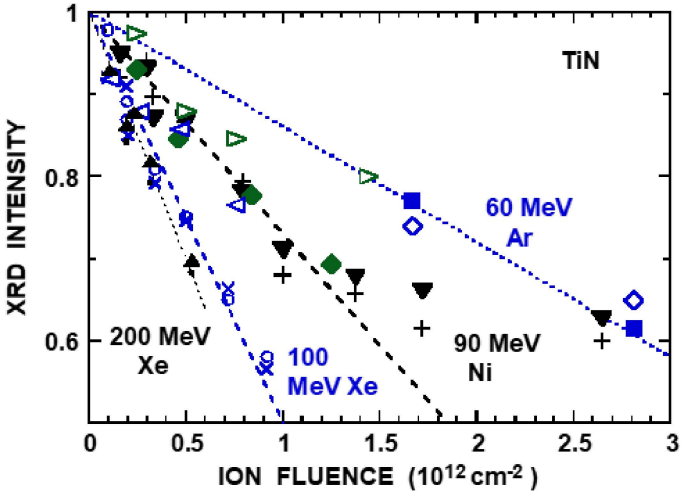

Figure 8. XRD intensity normalized to unirradiated films of TiN as a function of ion fluence for 60 MeV Ar (■, ◊), 90 MeV Ni (▼, +, ♦, ⋂), 100 MeV Xe (o, x, ◁) and 200 MeV Xe (▲, •) ions. Diffraction plane (111) at diffraction angle of ~36.6° is indicated by ■, ▼, o and ▲ for SiO_2 substrate, (200) at ~43° by ◊, +, x and • for SiO_2 substrate, (111) by ♦ for C-Al_2O_3 substrate and (220) at ~61° by ⋂ and ◁ for R-Al_2O_3 substrate. Linear fit is indicated by dotted lines. An estimated error of XRD intensity is 10%.

Table 5. XRD data of TiN films. Ion, energy (E in MeV), XRD intensity degradation (Y_{XD}) for (111) and (200) diffraction on SiO_2 and C-Al_2O_3, substrates, Y_{XD} for (220) diffraction on R-Al_2O_3 in the parenthesis, E* = E − ΔE (energy loss in carbon foil of 100 nm) (MeV) and electronic (S_e*) and nuclear (S_n*) stopping powers in keV/nm and projected range R_p* (μm) calculated using SRIM2013 and sputtering yield Y_{sp} of Ti. S_e* (TRIM1997) is given in parenthesis.

Ion	Energy	Y_{XD}	E*	S_e*	S_n*	R_p*	Y_{sp}(Ti)
	(MeV)	(10^{-12} cm^2)	(MeV)	(keV/nm)	(keV/nm)	(μm)	
^{40}Ar	60	0.14	60	9.41 (9.33)	0.0135	7.6	51.8
^{58}Ni	90	0.27 (0.2)	89	15.5 (16.5)	0.0305	8.6	147
^{136}Xe	100	0.50 (0.35)	99	26.7 (25.5)	0.19	6.9	380
^{136}Xe	200	0.60	198	30.85 (30.25)	0.11	10	529

The characteristic length (L_{EQ}) is estimated to be 4.5, 4.4, 4.2 and 4.0 nm for 60 MeV Ar^{+7}, 90 MeV Ni^{+10}, 100 MeV Xe^{+14} and 200 MeV Xe^{+14}, respectively, from the empirical formula of the single-electron loss cross-section σ_{1L}(10^{-16} cm^2) of 0.43 (60 MeV Ar^{+7}), 0.44 (90 MeV Ni^{+10}), 0.46 (100 MeV Xe^{+14}) and 0.48 (200 MeV Xe^{+14}) [83,84]. Here, $\sigma_{1L} = \sigma_{1L}$(Ti) + σ_{1L}(N), and the ionization potential I_P and N_{eff} are (I_P = 143 eV and N_{eff} = 1) for Ar^{+7}, with those described in Section 3.1 for Ni^{+10} and Xe^{+14}. L_{EQ} is much smaller than the film thickness, and hence the charge-state effect is insignificant.

It is found that sputtered Ti collected in the carbon foil is proportional to the ion fluence, as shown in Figure 9 for 60 MeV Ar, 90 MeV Ni, 100 MeV Xe and 200 MeV Xe ions. The sputtering yield of Ti is obtained using the collection efficiency of 0.34 in the carbon foil collector [47] and the results are given in Table 5. Sputtered N collected in the carbon foil is obtained to be 0.4×10^{14} and 0.44×10^{14} cm^{-2} with an estimated error of 20% for 200 MeV Xe at 0.22×10^{12} cm^{-2} and 60 MeV Ar at 2.8×10^{12} cm^{-2}, respectively, and this is comparable with the Ti areal density of 0.4×10^{14} cm^{-2} (200 MeV Xe) and 0.475×10^{14} cm^{-2} (60 MeV Ar). The results imply stoichiometric sputtering, due to the collection efficiency of N in the carbon foil collector of 0.35 [55], which is close to that of Ti. Thus, the total sputtering yield (Ti + N) is obtained by doubling Y_{sp} (Ti) in Table 5. The sputtering yields of TiN (Y_{EC}) due to elastic collisions can be estimated assuming that Y_{EC} is proportional to the nuclear stopping power. Here, the proportional constant is obtained to be ~1.6 nm/keV using the experimental yields of 0.527 (0.6 keV Ar) and 0.427 (0.6 keV N) [94] and 0.7 (0.5 keV Cd) [88]. Y_{sp}(TiN)/Y_{EC} ranges from 2.5×10^3 to 6×10^3. The XRD intensity degradations Y_{XD} and Y_{sp}(Ti + N) are plotted as a function of the electronic stopping power S_e in Figure 10. It appears that both fit to the power-law: $Y_{XD} = (0.0224S_e)^{1.26}$ and $Y_{sp} = (1.17S_e)^{1.95}$. The exponents are comparable for XRD intensity degradation and sputtering.

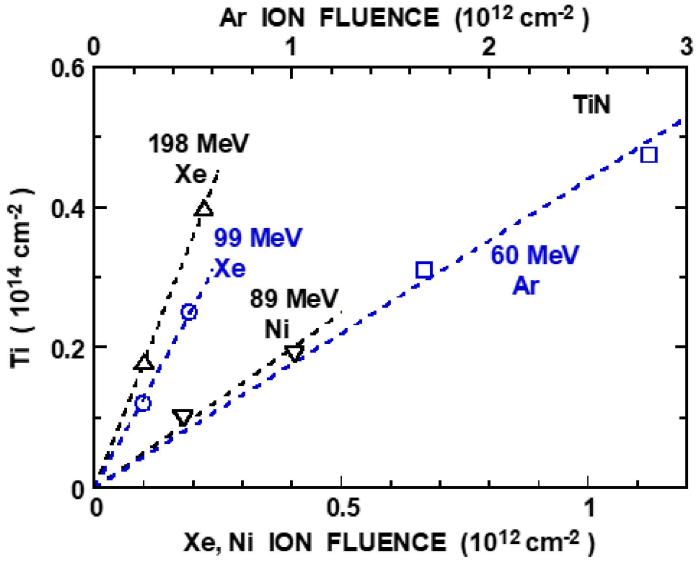

Figure 9. Areal density of sputtered Ti from TiN on SiO_2 substrate collected in carbon foil vs. ion fluence for 60 MeV Ar (□), 89 MeV Ni (∇), 99 MeV Xe (o) and 198 MeV Xe (Δ) ions. An estimated error of areal density is 20%.

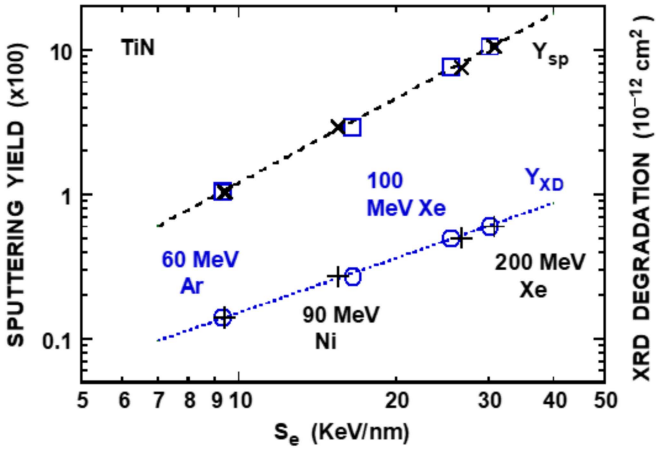

Figure 10. XRD intensity degradation Y_{XD} (10^{-12} cm^2) (o, +) and sputtering yields Ysp (Ti + N) (□, x) vs. electronic stopping power S_e (keV/nm). S_e is calculated by TRIM1997 (o, □) and by SRIM2013 (+, x). Power-law fits are indicated by dotted lines: $Y_{XD} = (0.0224S_e)^{1.26}$ and $Y_{sp} = (1.17S_e)^{1.95}$.

4. Discussion

4.1. Comparison of Lattice Disordering with Sputtering

The electronic stopping power (S_e) dependence of lattice disordering Y_{XD}, together with electronic sputtering, is summarized in Table 6, recognizing that most of the data have used TRIM1997. Results using SRIM2013 and TRIM1997 are compared in Section 3. Both exponents of the power-law fits are similar for SiO_2, ZnO, Fe_2O_3, TiN and WO_3 films, as well as for KBr and SiC. As mentioned in Section 3, it can be seen that the exponent of the lattice disordering N_{XD} is comparable with that of sputtering N_{sp}, except for Fe_2O_3, in which N_{sp} is exceptionally close to unity, as in the case of Cu_2O (N_{sp} = 1.0) [56] and CuO (N_{sp} = 1.08) [59]. The similarity of the exponent of lattice disordering and sputtering for SiO_2, ZnO, Fe_2O_3, TiN, WO_3, KBr and SiC imply that both phenomena originate from similar mechanisms, despite the fact that small displacements and annealing and/or the reduction in disordering via ion-induced defects are involved in the lattice disordering, whereas large displacements are involved in sputtering. The result of Fe_2O_3 indicates that the electronic excitation is more effective for lattice disordering. In

the case of CuO, N_{XD} is nearly zero [59]. In Table 6, Y_{XD} (10^{-12} cm^2) at S_e = 10 keV/nm and Y_{XD}/Y_{sp} ($\times 10^{-15}$ cm^2) are listed. It is found that the ratio Y_{XD}/Y_{sp} is an order of 10^{-15} cm^2, except for ZnO, where the sputtering yields are exceptionally small. More data of lattice disordering would be desired for further discussion.

Table 6. Summary of electronic stopping power (S_e in keV/nm) dependence of lattice disordering $Y_{XD} = (B_{XD}S_e)^{NXD}$ for the present results of SiO_2, ZnO, Fe_2O_3 and TiN films, and sputtering yields $Y_{sp} = (B_{sp}S_e)^{Nsp}$ of the present result for TiN. Lattice disordering and sputtering yields of WO_3 film from [58,72], those of KBr and SiC from [56] and sputtering yields of SiO_2, ZnO and Fe_2O_3 (see Section 3). Constant B_{XD} and B_{sp} and the exponent N_{XD} and N_{sp} are obtained using TRIM1997 and those using SRIM2013 are in parentheses. Y_{XD} at S_e = 10 keV and Y_{XD}/Y_{sp} (10^{-15} cm^2) are given.

Sample	B_{XD} (nm/keV)	N_{XD}	B_{sp} (nm/keV)	N_{sp}	Y_{XD} (10^{-12} cm^2) (S_e = 10 keV/nm)	Y_{XD}/Ysp (10^{-15} cm^2) (S_e = 10 keV/nm)
SiO_2	0.055 (0.0545)	3.4 (2.9)	0.58 (0.62)	3.0 (3.0)	0.13	0.67
ZnO	0.057 (0.0585)	1.32 (1.16)	0.175	1.57	0.476	198
Fe_2O_3	0.029 (0.028)	2.54 (2.28)	1.16 (2.2)	1.25 (1.05)	0.043	2.0
TiN	0.0224	1.26	1.17	1.95	0.15	1.26
WO_3	0.07355	2.65	0.65	3.6	0.44	0.53
KBr	0.127	2.4	0.77	3.0	1.78	3.9
SiC	0.0377	1.97	1.86	1.53	0.15	1.7

4.2. Electron–Lattice Coupling

Three models have been suggested for atomic displacement induced by electronic excitation: Coulomb explosion (CE) [3,4], thermal spike (TS) [50] and exciton model [30,95–97]. The neutralization time of the ionized region along the ion path is generally too short, and the fraction of the charged sputtered ions is small, e.g., 100 MeV Xe ions on SiO_2 glass [48]. Hence, the CE model is unsound. However, a small atomic separation during the short time might be enough for electron–lattice coupling (a key for electronic excitation effects), which will be discussed later. A crude estimation of the evaporation yield for SiO_2 based on the TS model appears to be far smaller than the experimental sputtering yield [55] and thus the TS model is also unsound. Moreover, the electron–lattice coupling or transfer mechanism of electronic energy into the lattice is not clear in the model. In the exciton model, the non-radiative decay of self-trapped excitons (STX, i.e., localized excited-state of electronic system coupled with lattice) leads to atomic displacement. According to the exciton model (or bandgap scheme), it is anticipated that the energy of the atoms in motion from the non-radiative decay of STX is comparable with the bandgap, leading to a larger sputtering yield with a larger bandgap, discarding the argument for the efficiency of STX generation from the electron–hole pairs, which is inversely proportional to the bandgap. This bandgap scheme is examined below. The effective depth contributing to the electronic sputtering of WO_3 has been obtained to be 40 nm, which is nearly independent of S_e [98], which would shed light on understanding the electronic sputtering; therefore, more data are desired.

The electronic sputtering yield Y_{sp} super-linearly depends on the electronic stopping power (S_e), and Y_{sp} at S_e = 10 keV/nm is taken to be a representative value, which is plotted as a function of the bandgap (E_g) in Figure 11 from [56], including the present TiN result. The optical absorbance (defined as $\log_{10}(I_o/I)$, I_o and I being the incident and transmitted photon intensities) of TiN films are measured, and the direct bandgap E_g is obtained to be 4.5 eV for a film thickness of 25–50 nm, which decreases to 2.8 eV for a film thickness of ~180 nm by using the relation: (absorbance • photon energy)^2 is proportional to photon energy—E_g. The thickness dependence of E_g is under investigation by considering the influence of the reflectivity, film growth conditions and experimental problems, such as stray light, etc. A large variation

has been reported for E_g, 4.0 eV (film thickness of 260 nm on Si substrate) (Popovic et al.) [99], 3.4 eV (thickness of ~100 nm on glass substrate) (Solovan et al.) [100] and 2.8–3.2 eV (film thickness of 460 nm on glass substrate) (Kavitha et al.) [101]. In this study, E_g is taken to be 4 eV and this choice is tolerable in the following discussion. It has been reported that the bandgap is reduced by 0.06 eV under a 400 KeV Xe ion implantation at 10^{16} cm^{-2} [99]. High-energy ion impact effects on optical properties are under way. It can be observed that the bandgap scheme seems to work for $E_g > 3$ eV [56]. A large deviation (two orders of magnitude) from the upper limit (dashed line indicated in Figure 11) is observed for ZrO_2, MgO, $MgAl_2O_4$ and Al_2O_3. The existence of STX is known for limited materials, rare gas solids, SiO_2 and alkali halides [30,95,96]. The STX does not exist for MgO and probably does not exist for Al_2O_3 [102]. The deviation for MgO and Al_2O_3 could be explained by the non-existence of STX. The numbers of electron–hole pairs leading to STX are inversely proportional to E_g, which could be a reason for the dependence of the sputtering yields for $E_g < 3$ eV. In any case, the single parameter of the band gap is insufficient for the explanation of the bandgap dependence of the sputtering yields.

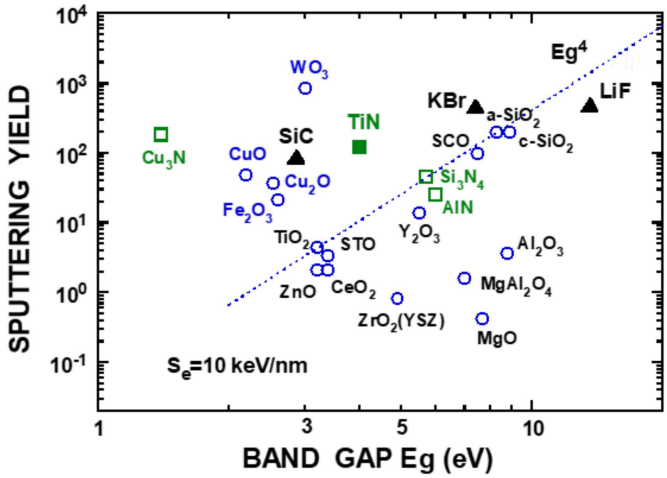

Figure 11. Sputtering yield at S_e = 10 keV/nm vs. bandgap. Data from [56], TiN (present result) and LiF data from [62]. Dotted line is a guide for eyes ($E_g > 3$ eV).

Martin et al. [102] argued that STX exists for materials with small elastic constants. Following this suggestion, sputtering yields are plotted as a function of the elastic constant (C_{11}) in Figure 12. Here, C_{11} (GPa) is taken to be 87 (SiO_2), 348 ($SrTiO_3$), 497 (Al_2O_3), 294 (MgO), 270 (TiO_2), 210 (ZnO), 299 ($MgAl_2O_4$), 242 (Fe_2O_3), 35 (KBr) and 114 (LiF) [85], and, for other materials, 403 (CeO_2) [103], 224 (Y_2O_3) [104], 400 (ZrO_2) [105], 13 (WO_3) [106], 126 (Cu_2O) [107], 135 (CuO) [108], 388 (Si_3N_4) as an average of the values [109,110], 345 (polycrystalline-AlN) [111], which is smaller by 16% than 410 (AlN single crystal) [112], 234 (Cu_3N) [113], 500 (SiC) [114] and 625 (TiN) [115]. It can be observed for oxides (the most abundant data are available at present) that Y_{sp} decreases exponentially with an increase in the elastic constant for $C_{11} < 300$ GPa, except for MgO and ZrO_2. Y_{sp} for nitrides and SiC is larger than that for oxides at a given C_{11}, and these are to be separately treated. It can be understood that the elastic constant represent the resistance of lattice deformation by electronic energy deposition. However, a single parameter, either the bandgap or elastic constant, is not adequate, and at least one more parameter is necessary. Furthermore, parameters other than those mentioned above are to be explored. More data for nitrides, alkali halides and especially carbides are desired.

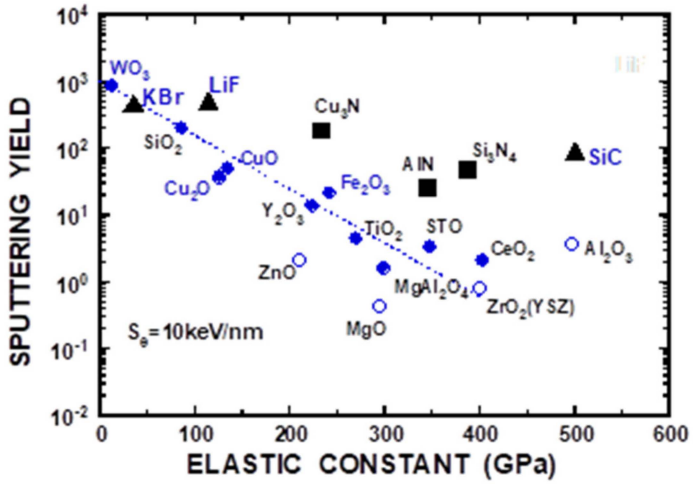

Figure 12. Sputtering yield at S_e = 10 keV/nm vs. elastic constant. Sputtering yield of TiN (present result), LiF from [62] and others from [56]. Dotted line is a guide for eyes for the most abundant available data of oxides (o, •).

Finally, a mechanism for the electron–lattice coupling is discussed. In an ionized region along the ion path, Coulomb repulsion leads to atomic motion, which is not adequate to cause sputtering because of its short neutralization time. Nevertheless, displacement comparable with the lattice vibration amplitude (one tenth of the average atomic separation, d_{av} of ~0.25 nm for a-SiO_2) is highly achievable during the neutralization time. As a first step, the time required for the Si^+–O^+ displacement of 0.025 nm (one tenth of d_{av}) from d_{av} is estimated to be ~15 fs using a formula [116]. Also, the time is estimated to be ~ 15 fs and ~ 12 fs for the Zn^+–O^+ displacement of 0.02 nm from d_{av} of 0.2 nm in ZnO and for the Ti^+–N^+ displacement of 0.02 nm from d_{av} of 0.2 nm in TiN, respectively. A similar situation has been reported for the Fe^+–O^+ displacement of 0.01 nm in Fe_2O_3 (~7 fs) [60], the K^+–Br^+ displacement of 0.01 nm in KBr (~9 fs) and the Si^+–C^+ displacement of 0.01 nm in SiC (~6 fs). These suggest a possibility that a small displacement comparable with the lattice vibration amplitude caused by Coulomb repulsion during the short neutralization time leads to the generation of a highly excited-state coupled with the lattice (h-ESCL), and h-ESCL is considered to be equivalent to STX or multi STX. The non-radiative decay of h-ESCL leads to atomic displacement (a larger displacement results in sputtering and smaller displacement results in phonon generation or lattice distortion).

5. Conclusions

We have measured the lattice disordering of polycrystalline SiO_2, ZnO, Fe_2O_3 and TiN films, as well as the sputtering yield of TiN, by high-energy ion impact. It is found that lattice disordering is caused by electronic excitation and the degradation of the XRD intensity fits to the power-law on the electronic stopping power. The exponent in the fit of the XRD degradation is comparable with that of the electronic sputtering yield for these films, as well as the published results of WO_3, KBr and SiC, implying that both lattice disordering and sputtering originate from similar mechanisms. In the case of Fe_2O_3, on the other hand, the exponent of the lattice disordering is larger by twice than that of the sputtering (the exponent for the sputtering is close to unity). The exciton mechanism seems to work for Eg > 3 eV, with some exceptions, and the elastic constant is examined as another scaling parameter for the electronic sputtering yields. A possibility of electron–lattice coupling is discussed based on a crude estimation that an atomic displacement comparable with the vibration amplitude due to Coulomb repulsion during the short neutralization time in the ionized region along the ion path can be attainable and, thus, the generation of a highly excited state coupled with the lattice is highly achievable, resulting in atomic displacement.

Author Contributions: Conceptualization and writing, N.M.; investigation, M.S., S.O. and B.T. All authors have read and agreed to the published version of the manuscript.

Funding: This research received no external funding.

Institutional Review Board Statement: Not applicable.

Informed Consent Statement: Not applicable.

Data Availability Statement: Not applicable.

Acknowledgments: One of the authors (N.M.) thanks for utilization of XRD equipments of RIGAKU ULTIMA IV and RAD IIc at Radioisotope Research Center, Nagoya University and of AN Van de Graaff accelerator, Nagoya University for Rutherford backscattering spectroscopy (RBS) measurement. High-energy ion irradiation has been performed using a TANDEM accelerator at Tokai Research Center, JAEA.

Conflicts of Interest: The authors declare no conflict of interest.

References

1. Young, D.A. Etching of Radiation Damage in Lithium Fluoride. *Nature* **1958**, *182*, 375–377. [CrossRef] [PubMed]
2. Silk, E.C.H.; Barnes, R.S. Examination of Fission Fragment Tracks with an Electron Microscope. *Phil. Mag.* **1959**, *4*, 970–972. [CrossRef]
3. Fleischer, R.L.; Price, P.B.; Walker, R.M. Ion Explosion Spike Mechanism for Formation of Charged-Particle Tracks in Solids. *J. Appl. Phys.* **1965**, *36*, 3645–3652. [CrossRef]
4. Fleischer, R.L. *Tracks to Innovation*; Springer: New York, NY, USA, 1998; pp. 1–193.
5. Meftah, A.; Brisard, F.; Costantini, J.M.; Dooryhee, E.; Hage-Ali, M.; Hervieu, M.; Stoquert, J.P.; Studer, F.; Toulemonde, M. Track formation in SiO_2 quartz and the thermal-spike mechanism. *Phys. Rev. B* **1994**, *49*, 12457–12463. [CrossRef]
6. Toulemonde, M.; Bouffard, S.; Studer, F. Swift heavy ions in insulating and conducting oxides: Tracks and physical properties. *Nucl. Instr. Meth. B* **1994**, *91*, 108–123. [CrossRef]
7. Ramos, S.M.M.; Bonardi, N.; Canut, B.; Bouffard, S.; Della-Negra, S. Damage creation in α-Al_2O_3 by MeV fullerene impacts. *Nucl. Instr. Meth. B* **1998**, *143*, 319–332. [CrossRef]
8. Skuratov, V.A.; Zinkle, S.J.; Efimov, A.E.; Havancsak, K. Surface defects in Al_2O_3 and MgO irradiated with high-energy heavy ions. *Surf. Coat. Technol.* **2005**, *196*, 56–62. [CrossRef]
9. Khalfaoui, N.; Stoquert, J.P.; Haas, F.; Trautmann, C.; Meftah, A.; Toulemonde, M. Damage creation threshold of Al_2O_3 under swift heavy ion irradiation. *Nucl. Instr. Meth. B* **2012**, *286*, 247–253. [CrossRef]
10. O'Connell, J.H.; Rymzhanov, R.A.; Skuratov, V.A.; Volkov, A.E.; Kirilkin, N.S. Latent tracks and associated strain in Al_2O_3 irradiated with swift heavy ions. *Nucl. Instr. Meth. B* **2016**, *374*, 97–101. [CrossRef]
11. Kluth, P.; Pakarinen, O.H.; Djurabekova, F.; Giulian, R.; Ridgway, M.C.; Byrne, A.P. Nanoscale density fluctuations in swift heavy ion irradiated amorphous SiO_2. *J. Appl. Phys.* **2011**, *110*, 123520. [CrossRef]
12. Benyagoub, A.; Toulemonde, M. Ion tracks in amorphous silica. *J. Mater. Res.* **2015**, *30*, 1529–1543. [CrossRef]
13. Zinkle, S.J.; Skuratov, V.A.; Hoelzer, D.T. On the conflicting roles of ionizing radiation in ceramics. *Nucl. Instr. Meth. B* **2002**, *191*, 758–766. [CrossRef]
14. Van Vuuren, A.J.; Ibrayeva, A.D.; Skuratov, V.A.; Zdorovets, M.V. Analysis of the microstructural evolution of silicon nitride irradiated with swift Xe ions. *Ceram. Int.* **2020**, *46*, 7155–7160. [CrossRef]
15. Kitayama, T.; Morita, Y.; Nakajima, K.; Narumi, K.; Saitoh, Y.; Matsuda, M.; Sataka, M.; Tsujimoto, M.; Isoda, S.; Toulemonde, M.; et al. Formation of ion tracks in amorphous silicon nitride films with MeV C_{60} ions. *Nucl. Instr. Meth. B* **2015**, *356–357*, 22–27. [CrossRef]
16. Mota-Santiago, P.; Vazquez, H.; Bierschenk, T.; Kremer, F.; Nadzri, A.; Schauries, D.; Djurabekova, F.; Nordlund, K.; Trautmann, C.; Mudie, S.; et al. Nanoscale density variations induced by high energy heavy ions in amorphous silicon nitride and silicon dioxide. *Nanotechnology* **2018**, *29*, 144004. [CrossRef]
17. Kucheyev, S.O.; Timmers, H.; Zou, J.; Williams, J.S.; Jagadish, C.; Li, G. Lattice damage produced in GaN by swift heavy ions. *J. Appl. Phys.* **2004**, *95*, 5360–5365. [CrossRef]
18. Mansouri, S.; Marie, P.; Dufour, C.; Nouet, G.; Monnet, I.; Lebius, H.; Benamara, Z.; Al-Douri, Y. Swift heavy ion effects in gallium nitride. *Int. J. Nanoelectron. Mater.* **2008**, *1*, 101–106.
19. Sall, M.; Monnet, I.; Moisy, F.; Grygiel, C.; Grygiel, C.; Jubolt-Leclerc, S.; Della-Negra, S.; Toulemonde, M.; Balanzat, E. Track formation in III-N semiconductors irradiated by swift heavy ions and fullerene and re-evaluation of the inelastic thermal spike model. *J. Mater Sci.* **2015**, *50*, 5214–5227. [CrossRef]
20. Moisy, F.; Sall, M.; Grygiel, C.; Ribet, A.; Balanzat, E.; Monnet, I. Optical bandgap and stress variations induced by the formation of latent tracks in GaN under swift heavy ion irradiation. *Nucl. Instr. Meth. B* **2018**, *431*, 12–18. [CrossRef]
21. Kamarou, A.; Wesch, W.; Wendler, E.; Undisz, A.; Rettenmayr, M. Swift heavy ion irradiation of InP: Thermal spike modeling of track formation. *Phys. Rev. B* **2006**, *73*, 184107. [CrossRef]

22. Ochedowski, O.; Osmani, O.; Schade, M.; Bussmann, B.K.; Ban-d'Etat, B.; Lebius, H.; Schleberger, M. Graphitic nanostripes in silicon carbide surfaces created by swift heavy ion irradiation. *Nat. Commun.* **2014**, *5*, 3913. [CrossRef] [PubMed]
23. Alencar, I.; Silva, M.R.; Leal, R.; Grande, P.L.; Papaleo, R.M. Impact Features Induced by Single Fast Ions of Different Charge-State on Muscovite Mica. *Atoms* **2021**, *9*, 17. [CrossRef]
24. Okubo, N.; Ishikawa, N.; Sataka, M.; Jitsukawa, S. Surface amorphization in Al_2O_3 induced by swift heavy ion irradiation. *Nucl. Instr. Meth. B* **2013**, *314*, 208–210. [CrossRef]
25. Grygiel, C.; Moisy, F.; Sall, M.; Lebius, H.; Balanzat, E.; Madi, T.; Been, T.; Marie, D.; Monnet, I. In-situ kinetics of modifications induced by swift heavy ions in Al_2O_3: Colour center formation, structural modification and amorphization. *Acta Mater.* **2017**, *140*, 157–167. [CrossRef]
26. Dhar, S.; Bolse, W.; Lieb, K.-P. Ion-beam induced amorphization and dynamic epitaxial recrystallization in α-quartz. *J. Appl. Phys.* **1999**, *85*, 3120–3123. [CrossRef]
27. Rymzhanov, R.A.; Medvedev, N.; O'Connell, J.H.; van Vuuren, A.J.; Skuratov, V.A.; Evolkov, A.E. Recrystallization as the governing mechanism of ion track formation. *Sci. Rep.* **2019**, *9*, 3837. [CrossRef]
28. Williams, J.S. Damage Formation, Amorphization and Crystallization in Semiconductors at Elevated Temperature. Chapter 6. In *Ion Beam Modification of Solids*; Wesch, W., Wendler, E., Eds.; Springer: Berlin, Germany, 2016; pp. 243–285.
29. Gupta, S.; Gehrke, H.G.; Krauser, J.; Trautmann, C.; Severin, D.; Bender, M.; Rothard, H.; Hofsass, H. Conducting ion tracks generated by charge-selected swift heavy ions. *Nucl. Instr. B* **2016**, *381*, 76–83. [CrossRef]
30. Itoh, N.; Duffy, D.M.; Khakshouri, S.; Stoneham, A.M. Making tracks: Electronic excitation roles in forming swift heavy ion tracks. *J. Phys. Condens. Matter* **2009**, *21*, 474205. [CrossRef]
31. Rogers, M.D. Mass Transport and Grain Growth induced by Fission Fragments in Thin Films of Uranium Dioxide. *J. Nucl. Mater.* **1965**, *16*, 298–305. [CrossRef]
32. Rogers, M.D. Ejection of Uranium Atoms from Sintered UO_2. *J. Nucl. Mater.* **1967**, *22*, 103–105. [CrossRef]
33. Nilsson, G. Ejection of Uranium Atoms from Sintered UO_2 by Fission Fragments in Different Gases and at Different Gas Pressures. *J. Nucl. Mater.* **1966**, *20*, 215–230. [CrossRef]
34. Meins, C.K.; Griffith, J.E.; Qiu, Y.; Mendenhall, M.H.; Seiberling, L.E.; Tombrello, T.A. Sputtering of UF_4 by High Energy Heavy Ions. *Rad. Eff.* **1983**, *71*, 13–33. [CrossRef]
35. Bouffard, S.; Duraud, J.P.; Mosbah, M.; Schlutig, S. Angular distribution of the sputtered atoms from UO_2 under high electronic stopping power irradiation. *Nucl. Instr. Meth. B* **1998**, *141*, 372–377. [CrossRef]
36. Schlutig, S. Contribution a L'etude de la Pulverisation et de L'endommagement du Dioxyde D'uranuim par les Ions Lourds Rapides. Ph.D. Thesis, University of Caen, Caen, France, March 2001.
37. Brown, W.L.; Lanzerotti, L.J.; Poate, J.M.; Augustyniak, W.M. "Sputtering" of Ice by MeV Light Ions. *Phys. Rev. Lett.* **1978**, *40*, 1027–1030. [CrossRef]
38. Brown, W.L.; Augustyniak, W.M.; Brody, E.; Cooper, B.; Lanzerotti, L.J.; Ramirez, A.; Evatt, R.; Johnson, R.E. Energy Dependence of the Erosion of H_2O Ice Films by H and He Ions. *Nucl. Instr. Meth.* **1980**, *170*, 321–325. [CrossRef]
39. Bottiger, J.; Davies, J.A.; L'Ecuyer, J.; Matsunami, N.; Ollerhead, R. Erosion of Frozen-Gas Films by MeV Ions. *Rad. Eff.* **1980**, *49*, 119–124. [CrossRef]
40. Baragiora, R.A.; Vidal, R.A.; Svendsen, W.; Schou, J.; Shi, M.; Bahr, D.A.; Atteberrry, C.L. Sputtering of water ice. *Nucl. Instr. Meth. B* **2003**, *209*, 294–303. [CrossRef]
41. Dartois, E.; Auge, B.; Boduch, P.; Brunetto, R.; Chabot, M.; Domaracka, A.; Ding, J.J.; Kamalou, O.; Lv, X.Y.; Rothard, H.; et al. Heavy ion irradiation of crystalline ice: Cosmic ray amorphisation cross-section and sputtering yield. *Astron. Astrophys.* **2015**, *576*, A125. [CrossRef]
42. Galli, A.; Vorburger, A.; Wurz, P.; Tulej, M. Sputtering of water ice films: A re-assessment with singly and doubly charged oxygen and argon ions, molecular oxygen, and electrons. *Icarus* **2017**, *291*, 36–45. [CrossRef]
43. Brown, W.L.; Lanzerotti, L.J.; Marcantonio, K.J.; Johnson, R.E.; Reimann, C.T. Sputtering of Ices by High Energy Particle Impact. *Nucl. Instr. Meth. B* **1986**, *14*, 392–402. [CrossRef]
44. Mejia, C.; Bender, M.; Severin, D.; Trautmann, C.; Boduch, P.H.; Bordalo, V.; Domaracka, A.; Lv, X.Y.; Martinez, R.; Rothard, H. Radiolysis and sputtering of carbon dioxide ice induced by swift Ti, Ni and Xe ions. *Nucl. Instr. Meth. B* **2015**, *365*, 477–481. [CrossRef]
45. Qiu, Y.; Griffith, J.E.; Meng, W.J.; Tombrello, T.A. Sputtering of Silicon and its Compounds in the Electronic Stopping Region. *Rad. Eff.* **1983**, *70*, 231–236. [CrossRef]
46. Sugden, S.; Sofield, C.J.; Murrell, M.P. Sputtering by MeV ions. *Nucl. Instr. Meth. B* **1992**, *67*, 569–573. [CrossRef]
47. Matsunami, N.; Sataka, M.; Iwase, A. Electronic sputtering of oxides by high energy ion impact. *Nucl. Instr. Meth. B* **2002**, *193*, 830–834. [CrossRef]
48. Matsunami, N.; Fukuoka, O.; Shimura, T.; Sataka, M.; Okayasu, S. A multi-exciton model for the electronic sputtering of oxides. *Nucl. Instr. Meth. B* **2005**, *230*, 507–511. [CrossRef]
49. Arnoldbik, W.M.; Tomozeiu, N.; Habraken, F.H.P.M. Electronic sputtering of thin SiO_2 films by MeV heavy ions. *Nucl. Instr. Meth. B* **2003**, *203*, 151–157. [CrossRef]
50. Toulemonde, M.; Assmann, W.; Trautmann, C.; Gruner, F. Jetlike Component in Sputtering of LiF Induced by Swift Heavy Ions. *Phys. Rev. Lett.* **2002**, *88*, 057602. [CrossRef]

51. Toulemonde, M.; Assmann, W.; Trautmann, C. Electronic sputtering of vitreous SiO_2: Experimental and modeling results. *Nucl. Instr. Meth B* **2016**, *379*, 2–8. [CrossRef]
52. Griffith, J.E.; Weller, R.A.; Seiberling, L.E.; Tombrello, T.A. Sputtering of Uranium Tetrafluoride in the Electronic Stopping Region. *Rad. Eff.* **1980**, *51*, 223–232. [CrossRef]
53. Toulemonde, M.; Assmann, W.; Muller, D.; Trautmann, C. Electronic sputtering of LiF, CaF_2, LaF_3 and UF_4 with 197 MeV Au ions: Is the stoichiometry of atom emission preserved? *Nucl. Instr. Meth. B* **2017**, *406*, 501–507. [CrossRef]
54. Matsunami, N.; Sataka, M.; Iwase, A.; Okayasu, S. Electronic excitation induced sputtering of insulating and semiconducting oxides by high energy heavy ions. *Nucl. Instr. Meth. B* **2003**, *209*, 288–293. [CrossRef]
55. Matsunami, N.; Sataka, M.; Okayasu, S.; Tazawa, M. Electronic sputtering of nitrides by high-energy ions. *Nucl. Instr. B* **2007**, *256*, 333–336. [CrossRef]
56. Matsunami, N.; Okayasu, S.; Sataka, M.; Tsuchiya, B. Electronic sputtering of SiC and KBr by high energy ions. *Nucl. Instr. Meth. B* **2020**, *478*, 80–84. [CrossRef]
57. Matsunami, N.; Sataka, M.; Okayasu, S.; Ishikawa, N.; Tazawa, M.; Kakiuchida, H. High-energy ion irradiation effects on atomic structures and optical properties of copper oxide and electronic sputtering. *Nucl. Instr. Meth. B* **2008**, *266*, 2986–2989. [CrossRef]
58. Matsunami, N.; Sataka, M.; Okayasu, S.; Kakiuchida, H. Ion irradiation effects on tungsten-oxide films and charge state effect on electronic erosion. *Nucl. Instr. Meth. B* **2010**, *268*, 3167–3170. [CrossRef]
59. Matsunami, N.; Sakuma, Y.; Sataka, M.; Okayasu, S.; Kakiuchida, H. Electronic sputtering of CuO films by high-energy ions. *Nucl. Instr. Meth. B* **2013**, *314*, 55–58. [CrossRef]
60. Matsunami, N.; Okayasu, S.; Sataka, M. Electronic excitation effects on Fe_2O_3 films by high-energy ions. *Nucl. Instr. Meth. B* **2018**, *435*, 142–145. [CrossRef]
61. Matsunami, N.; Kakiuchida, H.; Tazawa, M.; Sataka, M.; Sugai, H.; Okayasu, S. Electronic and atomic structure modifications of copper nitride films by ion impact and phase separation. *Nucl. Instr. Meth. B* **2009**, *267*, 2653–2656. [CrossRef]
62. Assmann, W.; d'Etat, B.B.; Bender, M.; Boduch, P.; Grande, P.L.; Lebius, H.; Lelievre, D.; Marmitt, G.G.; Rothard, H.; Seidl, T.; et al. Charge-state related effects in sputtering of LiF by swift heavy ions. *Nucl. Instr. Meth B* **2017**, *392*, 94–101. [CrossRef]
63. Toulemonde, M.; Assmann, W.; Ban-d'Etat, B.; Bender, M.; Bergmaier, A.; Boduch, P.; Della-Negra, S.; Duan, J.; El-Said, A.S.; Gruner, F.; et al. Sputtering of LiF and other halide crystals in the electronic energy loss regime. *Eur. Phys. J. D* **2020**, *74*, 144. [CrossRef]
64. Matsunami, N.; Sataka, M.; Okayasu, S.; Tsuchiya, B. Charge State Effect of High Energy Ions on Material Modification in the Electronic Stopping Region. *Atoms* **2021**, *9*, 36. [CrossRef]
65. Ziegler, J.F.; Biersack, J.P.; Littmark, U. *The Stopping and Range of Ions in Solids*; Pergamon Press: New York, NY, USA, 1985; pp. 1–321.
66. Ziegler, J.F.; Ziegler, M.D.; Biersack, J.P. SRIM-The stopping and range of ions in matter (2010). *Nucl. Instr. Meth. B* **2010**, *268*, 1818–1823. [CrossRef]
67. Grande, P.L.; Schiwietz, G. Convolution approximation for the energy loss, ionization probability and straggling of fast ions. *Nucl. Instr. Meth. B* **2009**, *267*, 859–865. [CrossRef]
68. Matsunami, N.; Sataka, M.; Iwase, A. Sputtering of high T_c superconductor $YBa_2Cu_3O_{7-\delta}$ by high energy heavy ions. *Nucl. Instr. Meth. B* **2001**, *175-177*, 56–61. [CrossRef]
69. Meftah, A.; Assmann, W.; Khalfaoui, N.; Stoquert, J.P.; Studer, F.; Toulemonde, M.; Trautmann, C.; Voss, K.-O. Electronic sputtering of $Gd_3Ga_5O_{12}$ and $Y_3Fe_5O_{12}$ garnets: Yield, stoichiometry and comparison to track formation. *Nucl. Instr. Meth. B* **2011**, *269*, 955–958. [CrossRef]
70. Shinde, N.S.; Matsuanmi, N.; Shimura, T.; Sataka, M.; Okayasu, S.; Kato, T.; Tazawa, M. Alignment of grain orientation in polycrystalline-SiO_2 films induced by high-energy heavy ions. *Nucl. Instr. Meth. B* **2006**, *245*, 231–234. [CrossRef]
71. Matsunami, N.; Itoh, M.; Kato, M.; Okayasu, S.; Sataka, M.; Kakiuchida, H. Ion induced modifications of Mn-doped ZnO films. *Nucl. Instr. Meht. B* **2015**, *365*, 191–195. [CrossRef]
72. Matsunami, N.; Kato, M.; Sataka, M.; Okayasu, S. Disordering of ultra thin WO_3 films by high-energy ions. *Nucl. Instr. Meth. B* **2017**, *409*, 272–276. [CrossRef]
73. Matsunami, N.; Sogawa, T.; Sakuma, Y.; Ohno, N.; Tokitani, M.; Masuzaki, S. Deuterium retention in Fe_2O_3 under low-energy deuterium-plasma exposure. *Phys. Scr. T* **2011**, *145*, 014042. [CrossRef]
74. Matsunami, N.; Ohno, N.; Tokitani, M.; Tsuchiya, B.; Sataka, M.; Okayasu, S. Modifications of WNOx films by keV D and H ions. *Surf. Coat. Technol.* **2020**, *394*, 125798. [CrossRef]
75. Matsunami, N.; Okayasu, S.; Sataka, M.; Tsuchiya, B. Ion irradiation effects on WN_xO_y thin films. *Nucl. Instr. Meth. B* **2018**, *435*, 146–151. [CrossRef]
76. Matsunami, N.; Teramoto, T.; Okayasu, S.; Sataka, M.; Tsuchiya, B. Modifications of WN_xO_y films by ion impact. *Surf. Coat. Technol.* **2018**, *355*, 84–89. [CrossRef]
77. Matsunami, N.; Itoh, M.; Takai, Y.; Tazawa, M.; Sataka, M. Ion beam modification of ZnO thin films on MgO. *Nucl. Instr. Meth. B* **2003**, *206*, 282–286. [CrossRef]
78. Matsunami, N.; Itoh, M.; Kato, M.; Okayasu, S.; Sataka, M.; Kakiuchida, H. Growth of Mn-doped ZnO thin films by rf-sputter deposition and lattice relaxation by energetic ion impact. *Appl. Surf. Sci.* **2015**, *350*, 31–37. [CrossRef]

79. Joint Committee on Powder Diffraction Standards (JCPDS). *JCPDS File 381420*; International Centre for Diffraction Data (ICDD): Newtown Square, PA, USA.
80. Storm, E.; Israel, H.I. Photon Cross Sections from 1 keV to 100 MeV for Elements Z = 1 to Z = 100. *Atom. Data Nucl. Data Tables* **1970**, *7*, 565–681. [CrossRef]
81. Shima, K.; Kuno, N.; Yamanouchi, M.; Tawara, H. Equilibrium Charge Fractions of Ions of Z = 4–92 Emerging from a Carbon Foil. *Atom. Data Nucl. Data Tables* **1992**, *51*, 173–241. [CrossRef]
82. Schiwietz, G.; Grande, P.L. Improved charge-state formulas. *Nucl. Instr. Meth B* **2001**, *175–177*, 125–131. [CrossRef]
83. DuBois, R.D.; Santos, A.C.F.; Olson, R.E. Scaling laws for electron loss from ion beams. *Nucl. Instr. Meth. A* **2005**, *544*, 497–501. [CrossRef]
84. DuBois, R.D.; Santos, A.C.F. Target-Scaling Properties for Electron Loss by Fast Heavy Ions (Chapter 8). In *Atomic Processes in Basic and Applied Physics*; Shevelko, V., Tawara, H., Eds.; Springer: Berlin, Germany, 2012; pp. 185–209.
85. Lide, D.R. (Ed.) *CRC Handbook of Chemistry and Physics*, 84th ed.; CRC Press: Boca Raton, FL, USA, 2003.
86. Rodrigues, G.C.; Indelicato, P.; Santos, J.P.; Patte, P.; Parente, F. Systematic calculation of total atomic energies of ground state configurations. *Atom. Data Nucl. Data Tables* **2004**, *86*, 117–233. [CrossRef]
87. Sigmund, P. Sputtering by Ion Bombardment: Theoretical Concepts. Chapter 2. In *Sputtering by Particle Bombardment*; Behrisch, R., Ed.; Springer: Berlin, Germany, 1981; Volume 1, pp. 9–71.
88. Betz, G.; Wehner, G.K. Sputtering of Multicomponent Materials. Chapter 2. In *Sputtering by Particle Bombardment*; Behrisch, R., Ed.; Springer: Berlin, Germany, 1983; Volume 2, pp. 11–90.
89. Paul, H. The Stopping Power of Matter for Positive Ions. Chapter 7. In *Modern Practices in Radiation Therapy*; Natanasabapathi, G., Ed.; InTech: Rijeka, Croatia, 2012; pp. 113–132.
90. Besenbacher, F.; Bottiger, J.; Graversen, O.; Hansen, J.L.; Sorensen, H. Stopping power of solid argon for helium ions. *Nucl. Instr. Meth.* **1981**, *188*, 657–667. [CrossRef]
91. Kittel, C. *Introduction to Solid State Physics*, 6th ed.; John Wiley & Sons Inc.: New York, NY, USA, 1986; pp. 1–646.
92. ICRU Report 49. *Stopping Powers and Ranges for Protons and Alpha Particles*; International Commission on Radiation Units and Measurements: Bethesda, MD, USA, 1993; pp. 1–286.
93. Arnau, A.; Bauer, P.; Kastner, F.; Salin, A.; Ponce, V.H.; Fainstein, P.D.; Echenique, P.M. Phase effect in the energy loss of hydrogen projectiles in zinc targets. *Phys. Rev. B* **1994**, *49*, 6470. [CrossRef]
94. Ranjan, R.; Allain, J.P.; Hendricks, M.R.; Ruzic, D.N. Absolute sputtering yield of Ti/TiN by Ar^+/N^+ at 400–700 eV. *J. Vac. Sci. Tech. A* **2001**, *19*, 1004–1007. [CrossRef]
95. Itoh, N. Creation of lattice defects by electronic excitation in alkali halides. *Adv. Phys.* **1982**, *31*, 491–551. [CrossRef]
96. Itoh, N.; Stoneham, A.M. *Materials Modification by Electronic Excitation*; Cambridge University Press: Cambridge, UK, 2001; pp. 1–520.
97. Duffy, D.M.; Daraszewicz, S.L.; Mulroue, J. Modeling the effects of electronic excitations in ionic-covalent materials. *Nucl. Instr. Meth. B* **2012**, *277*, 21–27. [CrossRef]
98. Matsunami, N.; Sataka, M.; Okayasu, S. Effective depth of electronic sputtering of WO_3 films by high-energy ions. *Nucl. Instr. Meth. B* **2019**, *460*, 185–188. [CrossRef]
99. Popovic, M.; Novakovic, M.; Mitric, M.; Zhang, K.; Rakocevic, Z.; Bibic, N. Xenon implantation effects on the structural and optical properties of reactively sputtered titanium nitride thin films. *Mat. Res. Bull.* **2017**, *91*, 36–41. [CrossRef]
100. Solovan, M.; Brus, V.V.; Maistruk, E.V.; Maryanchuk, P.D. Electrical and Optical Properties of TiN Films. *Inorgan. Mat.* **2014**, *50*, 40–45. [CrossRef]
101. Kavitha, A.; Kannan, R.; Reddy, P.S.; Rajashabala, S. The effect of annealing on the structural, optical and electrical properties of Titanium Nitride (TiN) thin films prepared by DC magnetron sputtering with supported discharge. *J. Mat. Sci. Mat. Electron.* **2016**, *27*, 10427–10434. [CrossRef]
102. Martin, P.; Guizard, S.; Daguzan, P.; Petite, G.; D'Oliveira, P.; Meynadier, P.; Perdrix, M. Subpicosecond study of carrier trapping dynamics in wide-band-gap crystals. *Phys. Rev. B* **1997**, *9*, 5799–5810. [CrossRef]
103. Nakajima, A.; Yoshihara, A.; Ishigame, M. Defect-induced Raman spectra in doped CeO_2. *Phys. Rev. B* **1994**, *50*, 13297–13307. [CrossRef]
104. Palko, J.W.; Kriven, W.M.; Sinogeikin, S.V.; Bass, J.D.; Sayir, A. Elastic constnts of yttria (Y_2O_3) monocrystals to high temperatures. *J. Appl. Phys.* **2001**, *89*, 7791–7796. [CrossRef]
105. Kandil, H.M.; Greiner, J.D.; Smith, J.F. Single-Crystal Elastic Constnats of Yttria-Stabilized Ziroconia in the Range 20° to 700 °C. *J. Am. Ceram. Soc.* **1984**, *67*, 341–346. [CrossRef]
106. Arab, M.; Dirany, N.; David, M. BAW resonator as elastic characterization tools of WO_3 thin films. *Mater. Today Proc.* **2016**, *3*, 152–156. [CrossRef]
107. Beg, M.M.; Shapiro, S.M. Study of phonon dispersion relations in cuprous oxide by inelastic neutron scattering. *Phys. Rev. B* **1976**, *13*, 1728–1734. [CrossRef]
108. Yao, B.; Zhou, X.; Liu, M.; Yu, J.; Cao, J.; Wang, L. First-principles calculations on phase transformation and elastic properties of CuO under pressure. *J. Comp. Electron.* **2018**, *17*, 1450–1456. [CrossRef]
109. Hay, J.C.; Sun, E.Y.; Pharr, G.M.; Becher, P.F.; Alexander, K.B. Elastic Anisotropy of β–Silicon Nitride Whiskers. *J. Am. Ceram. Soc.* **1998**, *81*, 2661–2669. [CrossRef]

110. Vogelgesang, R.; Grimsditch, M.; Wallace, J.S. The elastic constants of single crystal β–Si_3N_4. *Appl. Phys. Lett.* **2000**, *76*, 982–984. [CrossRef]
111. Carlotti, G.; Gubbiotti, G.; Hickernell, F.S.; Liaw, H.M.; Socino, G. Comparative study of the elastic properties of polycrystalline aluminum nitride films on silicon by Brillouin light scattering. *Thin Solid Films* **1997**, *310*, 34–38. [CrossRef]
112. McNeil, L.; Grimsditch, M.; French, R.H. Vibrational Spectroscopy of Aluminum Nitride. *J. Am. Ceram. Soc.* **1993**, *76*, 1132–1136. [CrossRef]
113. Hou, Z.F. Effects of Cu, N and Li interaction on the structural stability and electronic structure of cubic Cu_3N. *Solid State Sci.* **2008**, *10*, 1651–1657. [CrossRef]
114. Kamitani, K.; Grimsditch, M.; Nipko, J.C.; Loong, C.K.; Okada, M.; Kimura, I. The elastic constants of silicon carbide: A Brillouin-scattering study of 4H and 6H SiC single crystals. *J. Appl. Phys.* **1997**, *82*, 3152–3154. [CrossRef]
115. Kim, J.O.; Achenbach, J.D.; Mirkarimi, P.B.; Shinn, M.; Barnett, S.A. Elastic constants of single-crystal transition-metal nitride films measured by line-focus acoustic microscopy. *J. Appl. Phys.* **1992**, *72*, 1805–1811. [CrossRef]
116. Gemmell, D.S. Determining the Stereochemical Structures of Molecular Ions by "Coulomb-Explosion" Techniques with Fast (MeV) Molecular Ion Beams. *Chem. Rev.* **1980**, *80*, 301–311. [CrossRef]